Supplemental Document

optica

Observation of second-order meron polarization textures in optical microcavities: supplement

MATEUSZ KRÓL,[1] HELGI SIGURDSSON,[2,3] KATARZYNA RECHCIŃSKA,[1] PRZEMYSŁAW OLIWA,[1] KRZYSTOF TYSZKA,[1] WITOLD BARDYSZEWSKI,[4] ANDRZEJ OPALA,[5] MICHAŁ MATUSZEWSKI,[5] PRZEMYSŁAW MORAWIAK,[6] RAFAŁ MAZUR,[6] WIKTOR PIECEK,[6] PRZEMYSŁAW KULA,[7] PAVLOS G. LAGOUDAKIS,[2,3] BARBARA PIĘTKA,[1] AND JACEK SZCZYTKO[1,*]

[1]*Institute of Experimental Physics, Faculty of Physics, University of Warsaw, ul. Pasteura 5, PL-02-093 Warsaw, Poland*
[2]*Department of Physics and Astronomy, University of Southampton, Southampton SO17 1BJ, UK*
[3]*Skolkovo Institute of Science and Technology, Moscow, Russian Federation*
[4]*Institute of Theoretical Physics, Faculty of Physics, University of Warsaw, Warsaw, Poland*
[5]*Institute of Physics, Polish Academy of Sciences, al. Lotników 32/46, PL-02-668 Warsaw, Poland*
[6]*Institute of Applied Physics, Military University of Technology, Warsaw, Poland*
[7]*Institute of Chemistry, Military University of Technology, Warsaw, Poland*
[*]*Corresponding author: Jacek.Szczytko@fuw.edu.pl*

Supplement DOI: https://doi.org/10.6084/m9.figshare.13611410

Parent Article DOI: https://doi.org/10.1364/OPTICA.414891

Observation of second order meron polarisation textures in optical microcavities

MATEUSZ KRÓL,[1] HELGI SIGURDSSON,[2,3] KATARZYNA RECHCIŃSKA,[1] PRZEMYSŁAW OLIWA,[1] KRZYSTOF TYSZKA,[1] WITOLD BARDYSZEWSKI,[4] ANDRZEJ OPALA,[5] MICHAŁ MATUSZEWSKI,[5] PRZEMYSŁAW MORAWIAK,[6] RAFAŁ MAZUR,[6] WIKTOR PIECEK,[6] PRZEMYSŁAW KULA,[7] PAVLOS G. LAGOUDAKIS,[3,2] BARBARA PIĘTKA,[1] JACEK SZCZYTKO[1,*]

[1] *Institute of Experimental Physics, Faculty of Physics, University of Warsaw, ul. Pasteura 5, PL-02-093 Warsaw, Poland*
[2] *Department of Physics and Astronomy, University of Southampton, Southampton, SO17 1BJ, United Kingdom*
[3] *Skolkovo Institute of Science and Technology, Moscow, Russian Federation*
[4] *Institute of Theoretical Physics, Faculty of Physics, University of Warsaw, Poland*
[5] *Institute of Physics, Polish Academy of Sciences, al. Lotników 32/46, PL-02-668 Warsaw, Poland*
[6] *Institute of Applied Physics, Military University of Technology, Warsaw, Poland*
[7] *Institute of Chemistry, Military University of Technology, Warsaw, Poland*
[*] *Jacek.Szczytko@fuw.edu.pl*

1. Angle-resolved spectra corresponding to Berreman matrix simulations

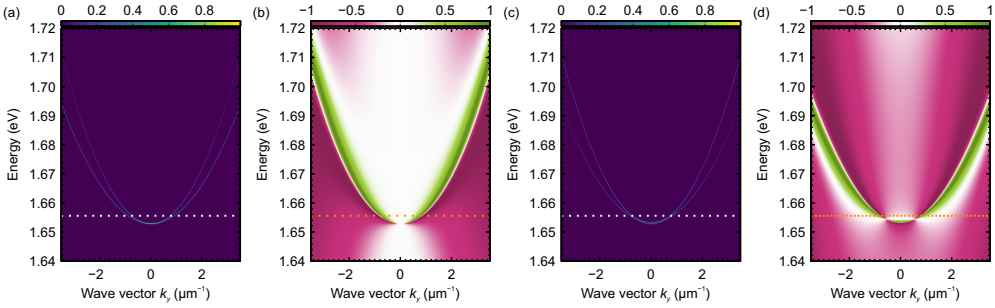

Fig. S1. Simulated angle-resolved transmittance corresponding to data in Fig. 3 in the main text. (a) Transmittance in (N, N) and (c) $(N + 2, N)$ regime. S_1 parameter of transmitted light in (b) (N, N) and (d) $(N + 2, N)$. Dashed vertical line marks energy of transmitted light resulting in spatial polarisation textures shown in Fig. 3 in the main tex.

Figure S1 presents simulated angle-resolved spectra corresponding to the data shown in Fig. 3 in the main text. Fig. S1(a) shows intensity of unpolarised light transmitted through the cavity in (N, N) regime [$\theta = 90°$, Fig. 2(a)–(d)]. We remind that θ is the angle of the liquid crystal (LC) molecular director. Fig. S1(b) presents corresponding S_1 Stokes parameter of transmitted light. Similarly Fig. S1(c),(d) depicts transmission intensity and S_1 Stokes parameter for $(N + 2, N)$ regime, which for this structure can be achieved by changing only molecules rotation angle to $\theta = 24.77°$.

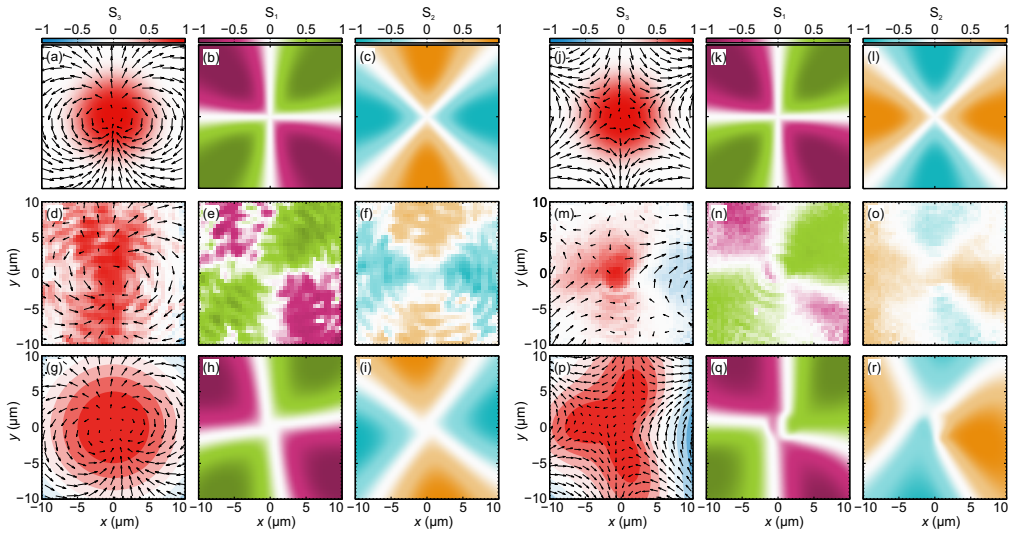

Fig. S2. Second order meron and antimeron textures in LC microcavities. (a)–(c), S_3, S_1, and S_2 Stokes parameters showing the analytical spin texture of a second order meron given by equation (3) in the main text. Black arrows correspond to $\mathbf{S}_{\parallel} = (S_1, S_2)$. (d)–(f) Experimental spatial polarisation texture of σ^+ polarised light transmitted through a LC microcavity in (N, N) regime. (g)–(i), Spatial polarisation texture calculated with the Berreman method. (j)–(l), S_3, S_1, and S_2 Stokes parameters showing the analytical spin texture of a second order antimeron given by equation (3) in the main text. (m)–(o), Experimental spatial polarisation texture of σ^+ polarised light transmitted through a LC microcavity in $(N+2, N)$ regime. (p)–(r), Spatial polarisation texture calculated with the Berreman method. Panels (a)–(f), (j)–(o) are a part of Fig. 4 from the main text.

2. Berreman matrix simulations of experimentally observed meron polarisation textures

Figure S2 presents Fig. 4 from the main text extended by Berreman matrix simulations of experimentally observed spatial polarisation textures in (N, N) regime [Fig. S2(g)–(i)] and in $(N + 2, N)$ regime [Fig. S2(p)–(r)]. Exact parameters of the simulated structures were optimised to match with experimental angle-resolved spectra for a given sample, shown in Fig. S3 and Fig. S4.

Figure S3(a),(b) presents experimental transmission intensity and S_1 parameter from cavity in (N, N) regime corresponding to data shown in Fig. S2(d)–(f). Fig. S3(c),(d) shows simulated spectra for a cavity that consists of two DBRs made of 5 pairs of layers with refractive indices $n_{\mathrm{low}} = 1.45$ and $n_{\mathrm{hi}} = 2.2$ centred at $\lambda_0 = 700$ nm. Simulated cavity is 1855 nm thick and filled with birefringent liquid crystal with $n_{\mathrm{o}} = 1.504$ and $n_{\mathrm{e}} = 1.801$ with director oriented along z direction.

Figure S4(a),(b) presents experimental transmission intensity and S_1 parameter from cavity in $(N+2, N)$ regime corresponding to data shown in Fig. S2(m)–(o). Fig. S4(c),(d) shows simulated spectra for a cavity that consists of two DBRs made of 4 pairs of layers with refractive indices n_{low} and n_{hi} centred at $\lambda_0 = 580$ nm. 1902 nm thick cavity is filled with birefringent liquid crystal with $n_{\mathrm{o}} = 1.539$ and $n_{\mathrm{e}} = 1.949$ with molecules rotation angle $\theta = 26.27$ deg.

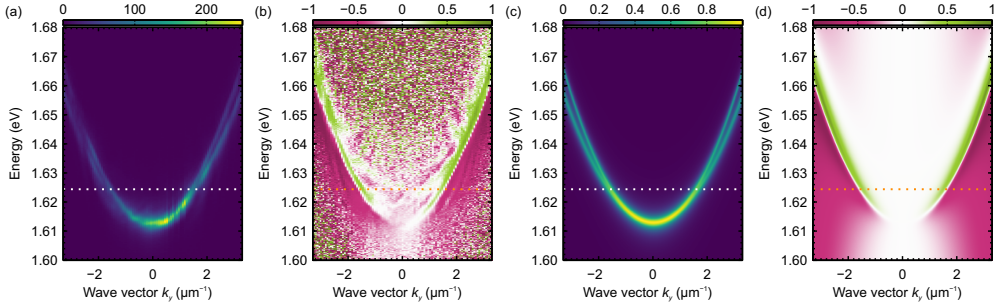

Fig. S3. Transmission from the (N, N) LC microcavity. (a) Experimental angle-resolved transmittance of white light through (N, N) LC microcavity. (b) S_1 stokes parameter of transmitted light. (c) Simulated angle-resolved transmittance of the cavity and (d) simulated S_1 Stokes parameter. Dotted horizontal lines mark energy of transmitted light resulting in spatial polarisation textures shown in Fig. S2(d)–(f) corresponding to experiment and Fig. S2(g)–(i) to simulation.

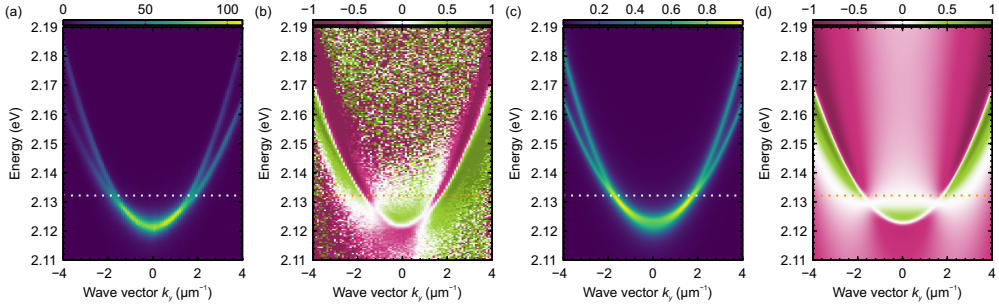

Fig. S4. Transmission from the $(N + 2, N)$ LC microcavity. (a) Experimental angle-resolved transmittance of white light through $(N + 2, N)$ LC microcavity. (b) S_1 stokes parameter of transmitted light. (c) Simulated angle-resolved transmission coefficient of the cavity and (d) simulated S_1 Stokes parameter. Dotted horizontal lines mark energy of transmitted light resulting in spatial polarisation textures shown in Fig. S2(m)–(o) corresponding to experiment and Fig. S2(p)–(r) to simulation.

3. Coupling of cavity modes in $(N + 2, N)$ regime

Figure S5 presents experimental angle-resolved transmittance spectra for a cavity tuned around $(N + 2, N)$ crossing (varying external voltage). Fig. S5(a)–(e) presents dispersion relation for wave vectors along x direction, Fig. S5(f)–(j) along y direction and Fig. S5(k)–(o) along diagonal direction. For wave vectors along the x and along y axes the X-polarised mode gradually crosses the Y-polarised mode. However for the antidiagonal wave vector direction ($k_x = -k_y$) an anticrossing behaviour between the modes can be observed, which is an evidence on coupling between them.

This anticrossing can be better illustrated in Fig. S6, showing transmission intensity at different voltages at a fixed 4.5 μm^{-1} wave vector value oriented in different directions: Fig. S6(a) for k_x, Fig. S6(b) for k_y, Fig. S6(c) for k_d and Fig. S6(d) for k_a. With wave vector along x and y directions are polarised accordingly to the main axes of LC molecules as shown in Fig. S6(e),(f) presenting intensity difference between X-polarised transmission intensity (I_X) and Y-polarised intensity (I_Y). At those directions modes crosses each other. Detection along the diagonal and antidiagonal directions [Fig. S6(c),(d)] reveals coupling between the modes observable as

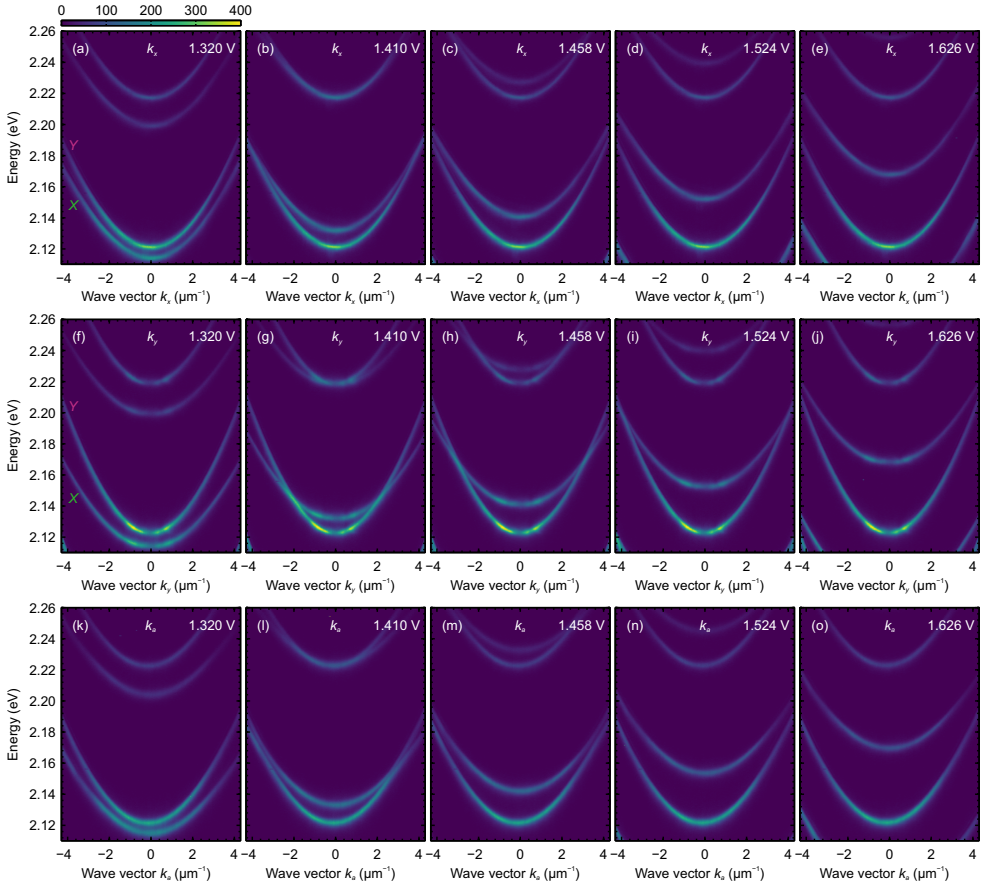

Fig. S5. Angle-resolved transmission intensity at different voltages applied to the LC microcavity around the $(N + 2, N)$ regime showing the gradual change in the system's dispersion properties. (a)–(e) Transmission angle along x axis: (a) 1.320 V, (b) 1.410 V, (c) 1.458 V (d) 1.524 V and (e) 1.626 V. The changing X polarised mode crosses over the unaffected Y polarised mode. (f)–(j) Transmission angle along y axis: (f) 1.320 V, (g) 1.410 V, (h) 1.458 V (i) 1.524 V and (j) 1.626 V. As previously, the changing X polarised mode crosses the unaffected Y polarised mode. (k)–(o) Transmission angle along antidiagonal (a) direction $(k_x = -k_y)$: (k) 1.320 V, (l) 1.410 V, (m) 1.458 V (n) 1.524 V and (o) 1.626 V. Increasing voltage now reveals the coupling between the modes observed as anticrossing behaviour.

anticrossing behaviour. For these wave vector orientations there is significant difference between intensity detected in diagonal (I_d) and antidiagonal (I_a) linear polarisations as presented in [Fig. S6(g),(h)]. Experimentally observed results are in a good agreement with Berreman matrix simulations shown in Fig. S6(i)–(l).

4. Meron orientation and size

Size and orientation of the meron polarisation texture depends on the exact properties of a given LC microcavity. Fig. S7 presents impact of the birefringence of LC layer. Berreman matrix simulations were performed for a cavity made of 5 distributed Bragg reflector (DBR) pairs of layers with refractive indices $n_\mathrm{low} = 1.45$ and $n_\mathrm{high} = 2.2$ and thickness $\lambda_0/4n_i$, where

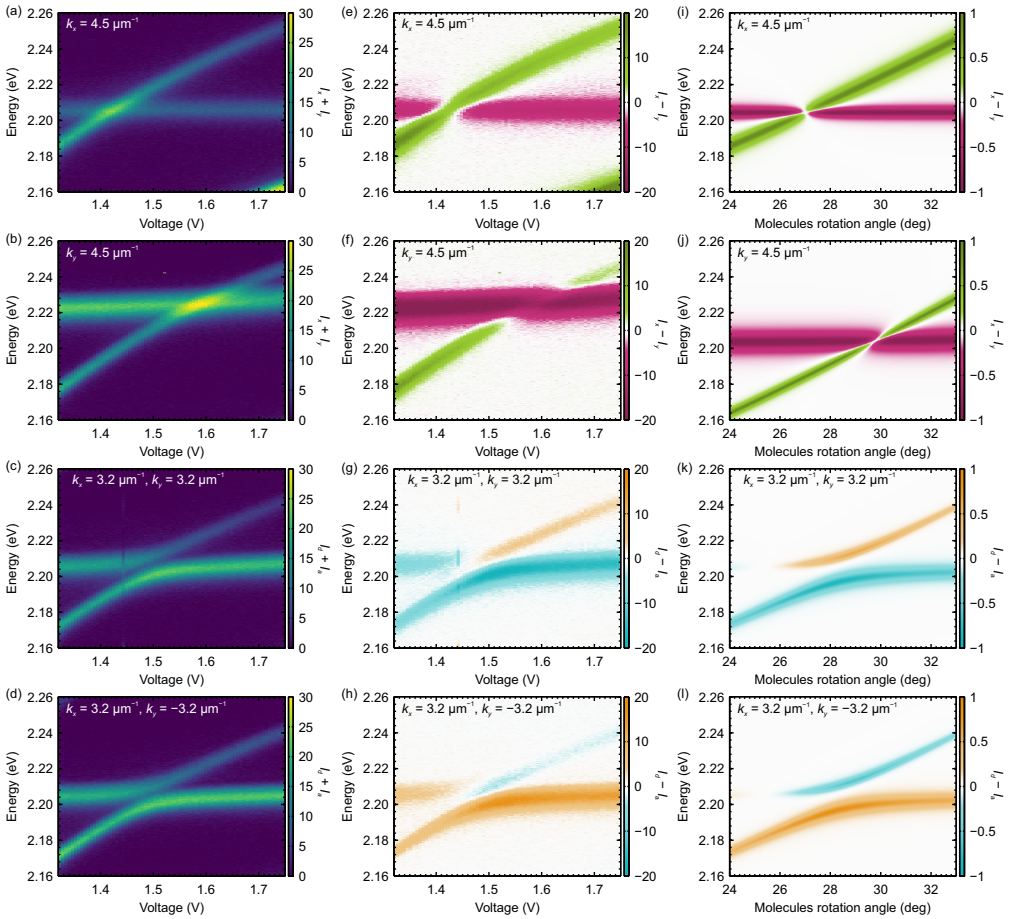

Fig. S6. Voltage tuning of LC microcavity in $(N+2, N)$ regime at 4.5 μm^{-1} wave vector at different directions. Total transmission intensity at (a) $k_x = 4.5\,\mu\text{m}^{-1}$, (b) $k_y = 4.5\,\mu\text{m}^{-1}$, (c) $k_d = 4.5\,\mu\text{m}^{-1}$ and (d) $k_a = 4.5\,\mu\text{m}^{-1}$. (e)–(f) Difference between transmission intensities of X- and Y-polarised light corresponding to [(a),(b)]. (g)–(h) Difference between transmission intensities of diagonally and antidiagonally polarised light corresponding to [(c),(d)]. (i)–(l) Corresponding simulated difference between transmittance in relevant polarisations with rotation of LC molecules director.

$\lambda_0 = 750\,\text{nm}$ (1.6531 eV). Central LC layer was simulated with $n_\text{o} = 1.504$ and thickness $5\lambda_0/n_\text{o}$, where n_e was changed to obtain different birefringence $\Delta n = n_\text{e} - n_\text{o}$. Fig. S7a–c presents simulated spatial polarisation textures of transmitted light obtained for σ^+ polarised incident beam with wavelength 748.9 nm (1.6556 eV) at different birefringences: Fig. S7(a) $\Delta n = -0.4$, Fig. S7b $\Delta n = -0.02$ and Fig. S7(c) $\Delta n = 0.4$. Corresponding angle-resolved reflectance spectra are presented in Fig. S7(d)–(f). With varying birefringence both spatial size and orientation of the second order meron polarisation texture changes, as summarised in Fig. S7(g). With increasing birefringence meron texture rotates clockwise with the steepest change when Δn is close to zero. Low optical anisotropy of the LC layer results also in increasing size of the meron texture. Due to low light intensity far away from the excitation spot simulation range is limited to $\approx \pm 100\,\mu\text{m}$.

Size and orientation of the meron textures depends also on the energy position of the mode within the photonic stopband region of the DBRs, which is summarised in Fig. S8. Calculations

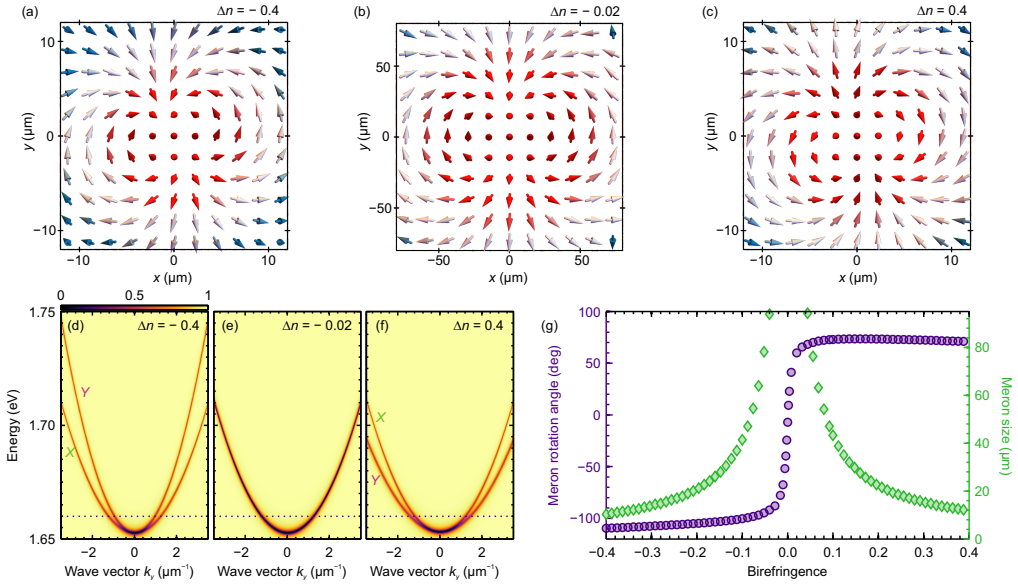

Fig. S7. Simulated dependence of the second order meron orientation and size on LC birefringence. Polarisation texture of transmitted light for (a) $\Delta n = -0.4$, (b) $\Delta n = -0.02$ and (c) $\Delta n = 0.4$. Note the flipped in-plane orientation of the arrows. Angle-resolved reflectance spectra for (d) $\Delta n = -0.4$, (e) $\Delta n = -0.02$ and (f) $\Delta n = 0.4$ where dashed line marks photon energy investigated in transmission. (g) Dependence of the size (radius) and orientation angle of a second order meron (diamonds and circles respectively) on LC birefringence.

were performed for analogous cavity as in Fig. S7, with $\Delta n = 0$. Energy of the mode is changed in simulations by adjusting thickness of the LC layer filling the cavity by −300 nm to 350 nm from initial value 2437 nm resulting in a cavity resonance at central wavelength λ_0. Such thickness range allows to tune cavity mode energy by ≈ 0.3 eV, as shown in the angle-resolved reflectance spectra in Fig. S8(d) for −165 meV, Fig. S8(e) for 0 meV, and Fig. S8(f) for 173 meV energy shifts from λ_0. The investigated mode in this multimode cavity is marked by a dashed line showing the transmitted light energy 10 meV above the mode resonance at normal incidence. Simulated second order antimeron textures are calculated for Fig. S8(a) −165 meV, Fig. S8(b) −52 meV and Fig. S8(c) for 173 meV energy shift from the central wavelength. Overall dependence of meron texture orientation and size on the cavity mode energy shift [Fig. S8(g)] follows qualitatively the same dependence as when varying the birefringence shown previously in Fig. S7(g).

5. Effective Hamiltonians for coupled X and Y polarised modes

The eigenmodes inside the cavity are represented by plane waves propagating in the plane of the cavity perpendicular to the z axis:

$$\begin{pmatrix} E_x(x,y,z) \\ E_y(x,y,z) \end{pmatrix} = \vec{E}_{\vec{k}}(z) e^{i(\vec{k}\cdot\vec{r}-\omega t)} \tag{S1}$$

The vector $\vec{E}_{\vec{k}}$ can by found from the following effective wave equation in the birefringent medium characterised by a dielectric tensor ϵ_{ij}:

$$-\partial_z^2 \vec{E} + \hat{A}\partial_z \vec{E} + \hat{B}_1 \vec{E} = k_0^2 \hat{B}_0 \vec{E} \tag{S2}$$

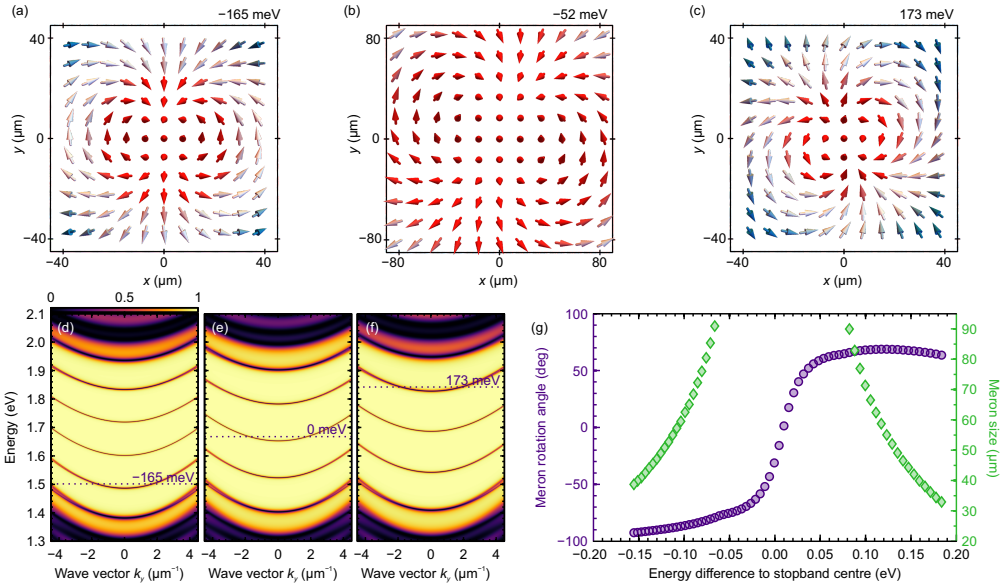

Fig. S8. Simulated dependence of second order meron orientation and size on energy position of the cavity mode within photonic stopband region. Polarisation texture of transmitted light for (a) −165 meV, (b) −52 meV and (c) 173 meV energy shift of the cavity mode from stopband centre. Angle-resolved reflectance spectra for (d) −165 meV, (e) 0 meV and (f) 173 meV energy shift of the cavity mode from stopband centre, where dashed line marks photon energy investigated in transmission. (g) Dependence of the size (radius) and orientation angle of a second order meron (diamonds and circles respectively) on cavity mode energy shift.

where $\vec{k} = \mathbf{k} = (k_x, k_y)$ and $k_0 = \omega/c$. Assuming that $\epsilon_{xy} = \epsilon_{yx} = \epsilon_{zy} = \epsilon_{yz} = 0$, we have up to the second order in k_x and k_y:

$$\hat{A} = \frac{-i\epsilon_{xz}}{\epsilon_{zz}} \begin{bmatrix} 2k_x & k_y \\ k_y & 0 \end{bmatrix}, \tag{S3}$$

$$\hat{B}_1 = \frac{1}{\epsilon_{zz}} \begin{bmatrix} \epsilon_{xx}k_x^2 + \tilde{\epsilon}_{zz}k_y^2 & (\epsilon_{yy} - \epsilon_{zz})k_y k_x \\ (\epsilon_{xx} - \tilde{\epsilon}_{zz})k_y k_x & \epsilon_{zz}k_x^2 + \epsilon_{yy}k_y^2 \end{bmatrix} \tag{S4}$$

and

$$\hat{B}_0 = \begin{bmatrix} \tilde{\epsilon}_{xx} & 0 \\ 0 & \epsilon_{yy} \end{bmatrix}. \tag{S5}$$

Here, $\epsilon_{yy} = n_o^2$ and for the given angle θ between the director of the LC molecules and the x axis we have

$$\begin{aligned} \tilde{\epsilon}_{xx} = n_{eff}^2 &= \frac{n_o^2 n_e^2}{n_o^2 \cos^2\theta + n_e^2 \sin^2\theta}, \\ \tilde{\epsilon}_{zz} &= \frac{n_{eff}^2 (n_o^4 \cos^2\theta + n_e^4 \sin^2\theta)}{n_o^2 n_e^2}, \end{aligned} \tag{S6}$$

and $\epsilon_{xz} = \epsilon_{zx} = (n_e^2 - n_o^2)\sin\theta\cos\theta$.

We wish to find the approximate dispersion relations of modes almost perfectly confined between the mirrors. Therefore the electric field is expanded as follows:

$$\vec{E}_{\vec{k}}(z) = \sum_{s=X,Y}\sum_{n=1}^{\infty} f_{sn}|s,n\rangle, \tag{S7}$$

where the basis states:

$$|X,n\rangle = (-1)^n\sqrt{\frac{2}{L}}\sin\left(\frac{n\pi}{L}z\right)\begin{bmatrix}1\\0\end{bmatrix}$$

and

$$|Y,n\rangle = (-1)^n\sqrt{\frac{2}{L}}\sin\left(\frac{n\pi}{L}z\right)\begin{bmatrix}0\\1\end{bmatrix} \tag{S8}$$

with $n = 1,2,3\ldots$, correspond to the electric field polarised parallel to the x and y axis, respectively. In this representation the matrix elements:

$$\langle sn|\partial_z^2|s'n'\rangle = -\frac{\pi^2}{L^2}n^2\delta_{nn'}\delta_{ss'}, \tag{S9}$$

$$\langle sn|\hat{B}_{1,0}|s'n'\rangle = (\hat{B}_{1,0})_{ss'}\delta_{nn'}. \tag{S10}$$

couple modes of the same order while the matrix elements

$$\langle sn|\hat{A}\partial_z|s'n'\rangle = (\hat{A})_{ss'}\begin{cases}\dfrac{4nn'}{L(n^2-n'^2)} & \text{for } n'+n \text{ odd},\\ 0 & \text{for } n'+n \text{ even}\end{cases} \tag{S11}$$

couple only modes with different parity.

At $k_x = k_y = 0$ we have simple modal solutions with the electric field $\vec{E}_{x,n} = |X,n\rangle$ polarised along the x axis with frequency $\omega_{Xn} = ck_{Xn} = c\pi n/(Ln_{eff})$ and $\vec{E}_{y,n} = |Y,n\rangle$ modes polarised along y direction with $\omega_{Yn} = ck_{Yn} = c\pi n/(Ln_o)$. The degeneracy of modes occurs when $\omega_{Xn} \approx \omega_{Yn} \approx \omega_0 = \sqrt{(\omega_{Xn}^2 + \omega_{Yn}^2)/2}$. In order to find the approximate dispersion relation for frequencies in the vicinity of ω_0 we solve the system of linear equations for expansion coefficients f_{sn}:

$$\sum_{s'=X,Y}\sum_{n'=1}^{\infty}(\hat{W})_{sn,s'n'}f_{s'n'} = 0 \tag{S12}$$

where

$$\begin{aligned}(\hat{W})_{sn,s'n'} = &\left(\frac{\pi^2}{L^2}n^2\delta_{ss'} + (\hat{B}_1)_{ss'} - k_0^2(\hat{B}_0)_{ss'}\right)\delta_{nn'}\\ &+ \langle sn|\hat{A}\partial_z|s'n'\rangle.\end{aligned} \tag{S13}$$

In the matrix form we have:

$$\hat{W}\cdot\vec{f} = 0. \tag{S14}$$

Note that the last term in Eq. (S13) is linear in $\vec{k}$ so the coupling of modes of different parity can be treated perturbatively. In particular, when the degenerate modes are of the same parity, for example $n = n' = N$ or $n = N$ and $n' = N+2$, this last term will lead to the correction of the

second order and higher in $\vec{k}$. In order to see this we can introduce the projection operator $\hat{P}$ on the modes of the same parity as N ($\hat{P}$-parity), and $\hat{Q}$ - the projection operator on the modes of opposite parity ($\hat{Q}$-parity). Then of course $\vec{f} = \hat{P}\cdot\vec{f} + \hat{Q}\cdot\vec{f}$ where the first term constitutes the dominant part of $\vec{f}$ and the other represents the admixture from the states of opposite parity. Since we are interested mainly in the dispersion relation, we are looking for the solution for the dominant part $\hat{P}\cdot\vec{f}$:

$$(\hat{P}\hat{W}\hat{P} - \hat{P}\hat{W}\hat{Q}(\hat{Q}\hat{W}\hat{Q})^{-1}\hat{Q}\hat{W}\hat{P})\vec{f} = 0. \tag{S15}$$

The matrix $\hat{Q}\hat{W}\hat{Q}$ is limited to the subspace of states with $\hat{Q}$-parity and so is its inverse $(\hat{Q}\hat{W}\hat{Q})^{-1}$. To the lowest (zeroth) order in $\vec{k}$:

$$((\hat{Q}\hat{W}\hat{Q})^{-1})_{sn,s'n'} = \delta_{ss'}\delta_{nn'}\frac{1}{\frac{\pi^2}{L^2}n^2 - k_0^2(\hat{B}_0)_{ss}}. \tag{S16}$$

The matrix $\hat{Q}\hat{W}\hat{P}$ which couples modes of different parity has the form:

$$(\hat{Q}\hat{W}\hat{P})_{sn,s'n'} = (\hat{A})_{ss'}\frac{4nn'}{L(n^2 - n'^2)}. \tag{S17}$$

The electric field in the vicinity of the degeneracy point can be approximated by:

$$\vec{E}_{\vec{k}}(z) = f_{Xm}|X,m\rangle + f_{Yn}|Y,n\rangle, \tag{S18}$$

and we can consider two situations.

1) The degeneracy of two modes of the same order $m = n = N$ occurs when $n_{eff} = n_o$, i.e., when $\epsilon_{xz} = 0$ and $\epsilon_{yy} = \epsilon_{xx}$. In this case the mode mixing term [eq. (S17)] is equal to zero and the effective equation for the vector $\vec{f} = (f_{XN}, f_{YN})^T$ is

$$\begin{bmatrix} (k_0^2 - k_{XN}^2)\epsilon_{xx} & 0 \\ 0 & (k_0^2 - k_{YN}^2)\epsilon_{xx} \end{bmatrix}\vec{f} = \frac{1}{\epsilon_{zz}}\begin{bmatrix} \epsilon_{xx}k_x^2 + \epsilon_{zz}k_y^2 & (\epsilon_{xx} - \epsilon_{zz})k_yk_x \\ (\epsilon_{xx} - \epsilon_{zz})k_yk_x & \epsilon_{zz}k_x^2 + \epsilon_{xx}k_y^2 \end{bmatrix}\vec{f}. \tag{S19}$$

2) In the case of degeneracy of two modes of different order but the same parity the mixing term is different from zero so the effective equation for $\vec{f} = (f_{XN+2}, f_{YN})^T$:

$$\begin{aligned}\sum_{n'=N+2,N}\sum_{s'=X,Y}\Bigg(\Bigg(\frac{\pi^2}{L^2}n^2\delta_{ss'} + (\hat{B}_1)_{ss'} - k_0^2(\hat{B}_0)_{ss'}\Bigg)\delta_{nn'} + \\ -\sum_{m''}^{\infty}{}'\sum_{s"=X,Y}\frac{16nn'm''^2(\hat{A})_{ss"}(\hat{A})_{s"s'}}{(n^2 - m''^2)(m''^2 - n'^2)(\pi^2m''^2 - L^2k_0^2(\hat{B}_0)_{s"s"})}\Bigg)f_{s'n'} = 0.\end{aligned} \tag{S20}$$

where the prime over summation sign means that only m'' with parity different from the parity of n and n' which is the same as the parity of N are included. In this way the denominator is always different form zero. Approximating $k_0 \approx k_{XN+2} = k_{Y,N}$ in the denominator of the last term and defining

$$Z^{\pm}_{n,n'} = Z^{\pm}_{n',n} = \sum_{m''}^{\infty}{}'\frac{16nn'm''^2}{\pi^2(n^2 - m''^2)(m''^2 - n'^2)(m''^2 - (N+1\pm1)^2)} \tag{S21}$$

we obtain the following equation for $\vec{f}$ in the case of the resonance of modes of the order $N+2$

and N:

$$\begin{bmatrix} (k_0^2 - k_{XN+2}^2)\tilde{\epsilon}_{xx} & 0 \\ 0 & (k_0^2 - k_{YN}^2)\epsilon_{yy} \end{bmatrix} \vec{f} =$$

$$= \frac{1}{\epsilon_{zz}} \begin{bmatrix} (\epsilon_{xx} + 4Z^+_{N+2,N+2}\frac{\epsilon_{xz}^2}{\epsilon_{zz}})k_x^2 + (\tilde{\epsilon}_{zz} + Z^-_{N+2,N+2}\frac{\epsilon_{xz}^2}{\epsilon_{zz}})k_y^2 & 2Z^+_{N+2,N}\frac{\epsilon_{xz}^2}{\epsilon_{zz}}k_xk_y \\ 2Z^+_{N+2,N}\frac{\epsilon_{xz}^2}{\epsilon_{zz}}k_xk_y & \epsilon_{zz}k_x^2 + (\epsilon_{yy} + Z^+_{N,N}\frac{\epsilon_{xz}^2}{\epsilon_{zz}})k_y^2 \end{bmatrix} \vec{f}. \tag{S22}$$

Note that the effective equations in the vicinity of the resonance of modes of the same order (N, N) [eq. (S19)] and for the case of different orders, $(N, N+2)$ [eq. (S22)] have similar structure. However the origin of the term proportional to k_xk_y, which is responsible for coupling between the modes is different in each situation. In the (N, N) case we have a direct coupling between the TE and TM modes whereas the coupling between modes of different order is of indirect character and is mediated by modes with opposite parity. By standard manipulations, both equations can be transformed into an eigenvalue problem with a Hamiltonian presented in the main text.

6. Spin structure and meron orientation from momentum-space Hamiltonian

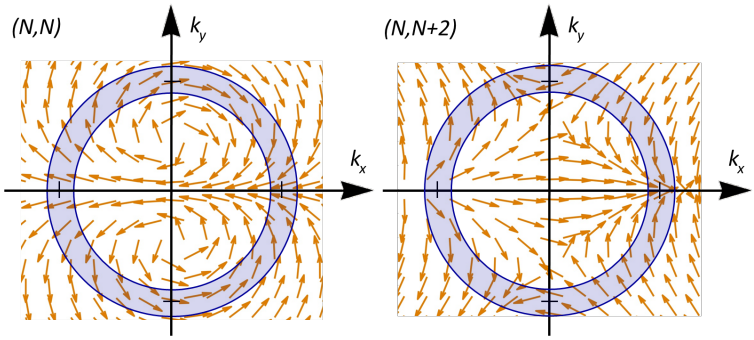

Fig. S9. Spin polarization from momentum-space Hamiltonian. The left and right panels show the spin polarization of one of the two eigenmodes of hamiltonian (2) in the main text (yellow arrows) in the meron and antimeron cases. The other mode has opposite polarization. The shaded ring depicts the approximate area in momentum space excited by a resonant laser beam. The polarization on the ring corresponds to the spin rotation in Fig. 3 in the main text.

The meron and antimeron spin structure results from transmission of light through cavity modes, which can be approximately described with Hamiltonian (2) in the main text. The emergence of such structures and the topological charge Q can be predicted from the eigenmodes of the Hamiltonian taking into account that the system is excited with resonant laser light with a Gaussian envelope in space. In Fig. S9 we show the spin polarisation of one of the Hamiltonian eigenmodes in the meron (N, N) and antimeron $(N+2, N)$ case. The shaded ring in momentum space corresponds to the approximate area excited with resonant light, which results from the parabolic dispersion relation of the cavity (see Fig. 2 in the main text). The second order meron spin structure of can be observed on this ring, and is retained after performing Fourier transform into real space, assuming that the excitation laser beam is Gaussian-shaped.

This simple explanation, however, is incomplete as it neglects the second, orthogonal eigenmode and does not explain the meron rotation angle discussed in the previous section. To take into

account the second mode, we estimate the amplitude and polarisation of light transmitted through microcavity. The amplitude of input light can be written as

$$\mathbf{A}_{\text{in}}(\mathbf{k}, \omega) = A(\mathbf{k})A(\omega)\mathbf{u}_{\text{in}}, \tag{S23}$$

where $A(\mathbf{k})$ is a Gaussian shaped amplitude, $A(\omega)$ is approximately δ-shaped laser frequency spectrum, $\mathbf{u}_{in}$ is the polarisation of input light, e.g. in linear polarization basis $\mathbf{u}_{in} = (1, 0)^T$ for a horizontally polarised light. In the considered cases (N, N) and $(N + 2, N)$ the cavity acts as a full-wave plate, so the polarisation of cavity mode at the output is not rotated by the cavity. The output amplitude is

$$\mathbf{A}_{\text{out}}(\mathbf{k}) = \sum_{i=1,2} t_i(\mathbf{k})A(\mathbf{k})P(\mathbf{u}_{\text{in}}, \mathbf{u}_i)\mathbf{u}_i, \tag{S24}$$

where we approximate the cavity transmission coefficient t as a sum of two eigenmodes $i = 1, 2$, each corresponding to a peak in transmission $t_i(\mathbf{k})$ with a similar amplitude and a Gaussian shape. The operator $P(\mathbf{u}_{\text{in}}, \mathbf{u}_i) = \mathbf{u}_{\text{in}} \cdot \mathbf{u}_i$ is the projection of input light polarisation on the eigenmode of the Hamiltonian (2) polarisation. The shape of $t_i(\mathbf{k})$ in momentum space is ring-like for each mode, with slightly differing radii. This results from the parabolic dispersion relation of the in-plane photonic cavity modes as shown in Fig. 3 in the main text.

Calculations of the above simplified Hamiltonian model are compared with Berreman method simulations in the case of $(N + 2, N)$ antimeron with σ^+ excitation in Fig. S10. The approximate 45 degrees orientation of the antimeron results from the overlap of the two rings in momentum space, with the phase of the transmission coefficients t_i differing by $\pi/2$. Such phase difference is explained by the dependence of the phase of the transmission coefficient on transverse momentum. This additional phase shift leads to rotation of input circular polarisation into horizontal or vertical polarisation in the diagonal directions ($k_x = \pm k_y$), which results in the whirling polarisation structure in momentum space and the corresponding rotation of the meron orientation.

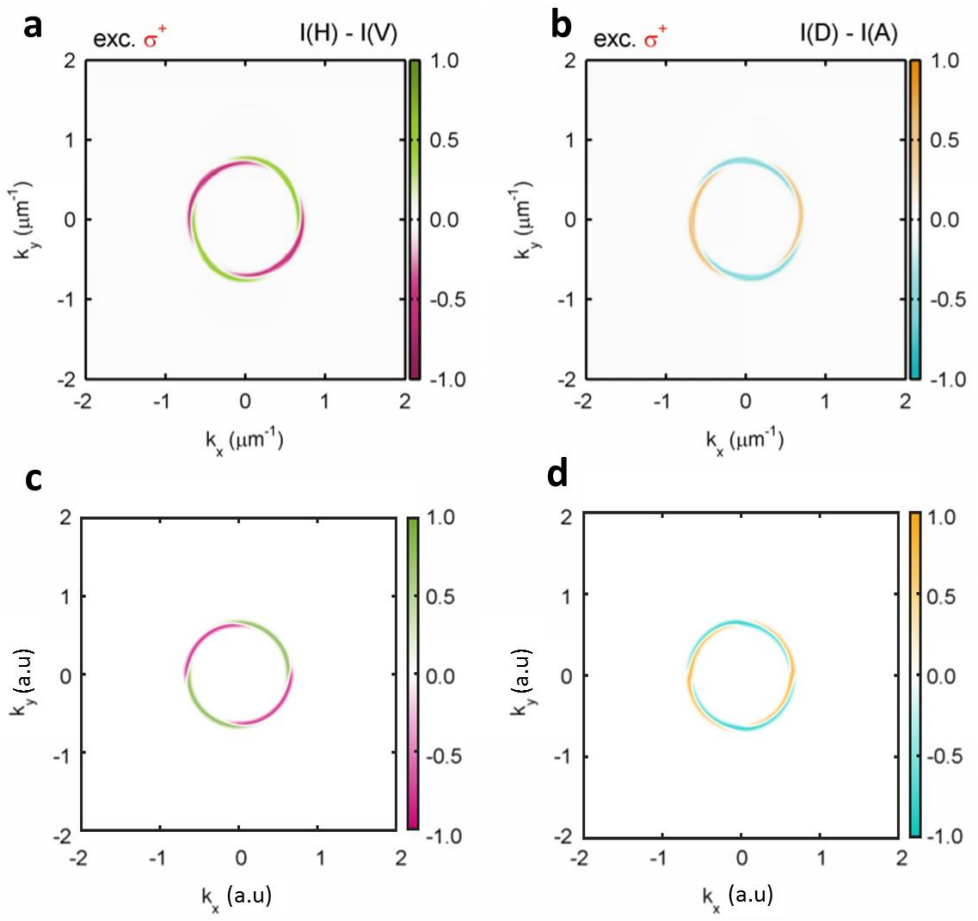

Fig. S10. Polarisation of transmitted light in momentum space. The top panels show the results of the Berreman method and the bottom panels the approximate Hamiltonian (2) in the case of circular input polarisation. The mixing of two modes with orthogonal polarisations (corresponding to rings with slightly different radii) results in rotation of the input polarisation in the diagonal directions ($k_x = \pm k_y$), which transforms the input circular polarisation into horizontal or vertical one between the rings. This leads to a helical structure of modes visible both in X-Y (left) and A-D polarisation patterns and the rotation of orientation by approximately 45 degrees.